Composites: Part A 210 (2026) 110071

Contents lists available at ScienceDirect

Composites Part A

journal homepage: www.elsevier.com/locate/compositesa

Process simulation of LFT-D compression molding with flow-orientation coupling and process-induced initial conditions

Louis Schreyer *, Florian Wittemann, Luise Kärger *

Lightweight Engineering, Institute of Vehicle System Technology (FAST), Karlsruhe Institute of Technology (KIT), Karlsruhe, 76131, Germany

ARTICLE INFO

Keywords:
Long fiber reinforced thermoplastic
Void content
Molding simulation
Skewed flow front

ABSTRACT

Long fiber reinforced thermoplastics compression molding with direct in-line compounding (LFT-D) has gained increased popularity for semi-structural components. Yet process simulation that accounts for the material's irregular initial conditions at the onset of molding remains largely unexplored. In particular, experimental work in the literature has shown that the flow front during compression molding of plates exhibits a pronounced skewness, which is attributed to the plastificate's spatially varying void-content distribution along the extrusion direction. In addition, the initial fiber orientation field is highly anisotropic and spatially varying, resulting in anisotropic macroscopic flow behavior. In this work, we present a methodology to incorporate this initial condition into a two-way flow–orientation coupled simulation framework for LFT-D compression molding considering a no-slip boundary condition. The experimentally determined void-content distribution is modeled through a geometric approach that scales the plastificate height, and the three-dimensional initial fiber orientation field is prescribed using a geometric generation methodology. The framework is applied to parallel plate compression molding with lateral plastificate positioning of a CF-PA6 LFT-D, and the predicted fiber orientations are compared with experimental observations. The simulations confirm that the inhomogeneous void content is a major contributing factor to the skewed flow front.

1. Introduction

1.1. Motivation and state of the art

Compression molded long fiber reinforced thermoplastics (LFT) have gained significant prominence in recent decades, particularly in the automotive industry. A notable potential application is in electric vehicle battery housings, driven by the sector's transition towards electrification. These materials offer superior mechanical properties compared to injection molded thermoplastic components due to the increased fiber length, making them suitable for (semi-)structural components. Moreover, due to the thermoplastic matrix, LFTs are in principle mechanically recyclable by remelting and reprocessing [1–3], addressing the increasing demand for sustainability and circular economy integration.

Direct in-line compounding of long fiber reinforced thermoplastics (LFT-D) offers increased design flexibility over pellet-based LFT by tailoring the material composition to specific component requirements. This process comprises two consecutive co-rotating twin screw extruders. The first extruder liquefies the polymer granulate and mixes it with the additives. In the second extruder, continuously fed fiber rovings are compounded with the molten thermoplastic matrix material. The compounded material is then pushed through the second extruder's rectangular nozzle and cut to length. During this process, fiber rovings break and disperse due to substantial shearing induced by the extruder screws. The bulk semi-finished material, referred to as plastificate in this work, is transferred immediately to the press for compression molding. Schematics of in-line compounding are available in, e.g., [4, 5].

Anisotropic viscosity modeling. LFT-D exhibits highly anisotropic macroscopic properties [6,7] resulting from the anisotropic and spatially varying fiber orientation field, making prediction of fiber reorientation during manufacturing crucial. Importantly, fibers not only reorient following the velocity field but also influence it, as demonstrated experimentally for LFT-D [5] and related systems such as glass mat thermoplastics (GMT) [8–10] and bundle-like thermoplastics [11]. This flow–orientation coupling, governing the anisotropic material response on the macroscopic scale, is typically modeled using anisotropic viscosity models [12–15]. Such models have been successfully applied to various discontinuous fiber reinforced materials [16–18]. For bulk LFT compression molding, previous numerical studies have exclusively employed isotropic viscosity models within commercial molding frameworks [19–21] or 2.5D in-house code [22], all limited to one-way

* Corresponding authors.
E-mail addresses: louis.schreyer@kit.edu (L. Schreyer), luise.kaerger@kit.edu (L. Kärger).

https://doi.org/10.1016/j.compositesa.2026.110071
Received 12 April 2026; Received in revised form 18 June 2026; Accepted 30 June 2026
Available online 8 July 2026
1359-835X/

flow–orientation coupling. However, in our recent work [5], we characterized a LFT-D material and observed fiber-induced anisotropic flow in squeeze flow experiments.

Initial fiber orientation distribution. For consistent fiber orientation evolution modeling, the plastificate's spatial fiber orientation distribution resulting from in-line compounding must be considered [20,23]. This holds particularly when modeling anisotropic material behavior. The fiber orientation within the plastificate (at molding onset) has been characterized using µCT imaging in several studies for various materials: glass fiber reinforced polypropylene (GF-PP) LFT-D [20,24], carbon fiber reinforced polyamide six (CF-PA6) LFT-D [23], and CF-PA6 pellet LFT [21]. For twin-screw setups, the initial fiber orientation exhibits consistent characteristics across different materials and die geometries: a more isotropic orientation near the center, swirl-like patterns around extruder screws, circumferential orientation towards the perimeter, and a thin surface layer with fibers aligned in the extrusion direction. Given the nature of the extrusion flow, periodicity in the extrusion direction [20] and twofold symmetry of the plastificate cross section [23,25] are assumed in literature. Song et al. [20,25] mapped µCT-derived initial fiber orientation onto numerical meshes (within a one-way coupled finite volume framework), whereas we proposed a geometry-based methodology [23] to generate the initial fiber orientation distribution incorporating the aforementioned characteristics.

Skewed flow front and void content. Despite advances in understanding and modeling initial fiber orientation, experimental observations reveal phenomena unexplained by fiber orientation alone. Notably, the skewed flow front observed experimentally in LFT-D compression molding [6,26,27] cannot be attributed solely to fiber-induced anisotropy and three-dimensional initial fiber orientation. Several studies report that the principal fiber direction deviates from expectations during molding of planar parts with lateral plastificate positioning (GF-PP [28]; CF-PA6 and GF-PA6 [6,29]), which is clearly reflected in the resulting macroscopic mechanical properties [6,30]. In a recent work [27], we identified the density distribution as a contributing factor: the effective density of the plastificate that first exits the extruder (the old end) is lower than that of the new end. This density gradient's influence on flow behavior has been investigated numerically within an uncoupled built-in finite element framework (Moldflow) with qualitative material parameters [27]. In addition, we made purely qualitative assumptions on the density, assuming a linear increase along the extrusion axis. This density difference is corroborated by void-content distribution measurements of the plastificate [29]. Note that the void content directly determines the effective density, making both quantities equivalent representations of the same physical phenomenon. A temperature gradient along the plastificate's surface has been reported in [26]; however, no significant temperature gradient exists within the plastificate at the onset of molding [27]. This rules out the initial temperature distribution as a major contributing factor. Furthermore, we ruled out geometric deviations in the tool through a comprehensive parameter study [27]. A first investigation into the influence of extruder settings, specifically the nozzle height and nozzle temperature of the second extruder, on the plastificate microstructure and the formation of a skewed flow front has been carried out in [31]. A coupled simulation framework combining anisotropic viscous behavior, three-dimensional initial fiber orientation distribution, and initial void distribution has yet to be established.

1.2. Originality

We introduce a two-way flow–orientation coupled simulation approach for LFT-D compression molding, which simultaneously accounts for the material's anisotropic nature and the plastificate's inhomogeneous initial material state at the onset of molding. Building on the purely synthetic void-content modeling in [27], we present a methodology that considers the spatially varying void-content distribution of the physical plastificate. To this end, we determine and analyze the void-content distribution along the extrusion axis based on available µCT data of an LFT-D plastificate [29]. As the plastificate's initial fiber orientation is crucial for modeling anisotropic behavior, we revisit the initial fiber orientation state both experimentally and from a modeling perspective, employing the geometry-based generation methodology previously introduced in [23]. Based on parallel plate compression molding, we investigate the influence of orientation-dependent viscosity and void-content distribution on the flow pattern and fiber orientation evolution, comparing results with experimental observations. The main contributions of this work are summarized as follows:

- A two-way flow–orientation coupled non-Newtonian simulation methodology for LFT-D compression molding considering no-slip boundary conditions.
- Consideration of the experimentally determined void-content distribution and the initial fiber orientation distribution.

The remainder of the work is structured as follows: Section 2 begins with a description of the investigated material system, followed by the presentation of the experimental flow study. Then, the plastificate's void content and the initial fiber orientation are analyzed. In Section 3, the macroscopic simulation methodology for LFT-D compression molding is presented, comprising a revisit of the governing equations, the anisotropic viscous material model, the approach for modeling the plastificate's initial fiber orientation, and the novel methodology for considering the void-content distribution through an initial height field. The section concludes with the definition of the simulation model and boundary conditions. In Section 4, the simulation results are presented, including a mesh convergence study and an investigation of the influence of anisotropy coupling. Section 5 discusses the results and Section 6 contains the conclusion and outlook.

1.3. Notation

This manuscript uses symbolic tensor notation. Bold lowercase letters denote vectors (e.g., $\boldsymbol{a}$), bold uppercase letters denote second-order tensors (e.g., $\boldsymbol{A}$), and double-struck letters denote fourth-order tensors (e.g., $\mathbb{A}$). For tensor contractions of equal order, we write, e.g., $(\boldsymbol{A}\boldsymbol{B})_{ij} = A_{ik}B_{kj}$. The linear mapping of a fourth-order tensor on a second-order tensor is expressed as $(\mathbb{A}[\boldsymbol{B}])_{ij} = A_{ijkl}B_{kl}$. For the scalar product, we write, e.g., $\boldsymbol{A} \cdot \boldsymbol{B} = A_{ij}B_{ij}$. The dyadic product is expressed as, e.g., $(\boldsymbol{a} \otimes \boldsymbol{b})_{ij} = a_i b_j$, and $(\cdot)^{\otimes i}$ denotes the ith time dyadic product. The second-order identity tensor is denoted by $\boldsymbol{I}$, and the fourth-order projection tensor onto symmetric deviatoric tensors is denoted by $\mathbb{I}^{\text{dev}}$.

2. Experiments

This section presents the experimental flow study and the characterization of the LFT-D plastificate, focusing specifically on the void content and fiber orientation. The LFT-D composite under investigation consists of Zoltek PX3505015W61 carbon fibers (CF, $d_\text{f} \approx 7.2\,\mu\text{m}$) and polyamide 6 (PA6) with the trade name DOMO Technyl Star XY 1352 BL Natural, which has been utilized in several related studies [5,6,23,29]. The nominal fiber volume content φ_f is approximately 26 %, and the arithmetic mean fiber length $\bar{l}_\text{f}$ is 1.6 mm [6]. Given the material's fiber volume content and mean fiber aspect ratio ($\bar{r}_\text{f} = \bar{l}_\text{f}/d_\text{f} \approx 222$), the investigated composite is considered concentrated. A detailed description of the in-line twin-screw extruder setup (with co-rotating extruder screws) and the corresponding screw configuration for plastificate manufacturing are given in [4,5,27].

2.1. Flow study and final fiber orientation

The flow study on CF-PA6 was conducted on a polished steel tool with a diving edge and dimensions 400 mm × 400 mm with lateral plastificate positioning. The rectangular die of the second twin screw extruder has a width of 75 mm and the height was set to 35 mm. The final part's nominal thickness is approximately three millimeters. To investigate the flow front evolution at different stages of compression, the flow path length was adjusted by increasing the final mold gap $h_{\min}$ through placing metal spacers between the mold halves. Consequently, each molding cycle provides a single contour. Four repetitions per final mold gap were performed. All molding trials were conducted at the Fraunhofer Institute for Chemical Technology (ICT) in Pfinztal, Germany, on a Dieffenbacher DYL 630/500 parallel-guided press.

The left graph in Fig. 1 shows the resulting contours (line style) at different adjusted final tool gaps (color). The red dashed outline indicates the initial position and dimensions of the plastificate at the onset of molding. The extrusion direction is indicated by an arrow, where the tip of the arrow points to the old end. The right graph in Fig. 1 shows the relative flow front skewness s_{ff} following [27] of the contours, which describes the relative deviation of the flow front's areal center in the 2-direction from the 1,3-plane at $x_2 = 200$ mm . The sign of s_{ff} encodes the skewness direction: $s_{\mathrm{ff}} < 0$ corresponds to a flow front tilted towards the positive x_3 direction (right-skewed), while $s_{\mathrm{ff}} > 0$ corresponds to a tilt in the negative x_3 direction (left-skewed). The colorings in the left and right graphs are identical. The results show the formation of a skewed flow front, i.e., the flow fronts are not symmetric with respect to the 1, 3-plane at $x_2 = 200$ mm and exhibit a distinct rotation around the out-of-plane 3-axis, which is reflected in s_{ff} and consistent with the results on GF-PA6 ($\varphi_{\mathrm{f}} \approx 19\,\%$; same PA6) reported in [27]. However, there are also realizations that exhibit little skewness (e.g., solid purple line at $h_{\min} = 5$ mm) or even an inverse skewness (e.g., dashed gray line at $h_{\min} = 4$ mm), which highlights the process-inherent scattering of LFT-D manufacturing. As discussed in Section 1.1, in a previous study [27], we ruled out geometric deviations in the tool and the temperature distribution within the plastificate (at the onset of molding) as causes of the skewed flow front, but identified the density distribution of the plastificate as a major contributing factor. Although PA6 is moisture-sensitive, moisture uptake is considered an unlikely source of the observed skewness, as the PA6 was preconditioned according to the manufacturer's instructions, and the transfer from the heated, insulated conveyor belt to the press offers minimal opportunity for water intake.

In addition to the flow front analysis, the final fiber orientation distribution is investigated using data from Scheuring et al. [6], who determined the fiber orientation on 25 mm × 25 mm × 3 mm samples at nine positions extracted from a plate molded with the same material and process settings. The fiber orientation is described by the ith (even) order fiber orientation tensor $\boldsymbol{A}_{\langle i\rangle}$ [32,33], which represents the statistical moments of the fiber orientation distribution function $\Psi(\boldsymbol{p})$, with $\boldsymbol{p} \in \mathcal{S}^2$, where $\boldsymbol{p}$ represents a fiber's orientation vector, and $\mathcal{S}^2$ denotes the unit sphere. The ith order fiber orientation tensor is defined as:

$$\boldsymbol{A}_{\langle i\rangle} = \int_{\mathcal{S}^2} \Psi(\boldsymbol{p})\boldsymbol{p}^{\otimes i}\,\mathrm{d}S, \tag{1}$$

where $(\cdot)^{\otimes i}$ denotes the i-fold dyadic product. Since fiber evolution equations typically employ the second-order fiber orientation tensor, we restrict our analysis to this order. Fig. 2 shows the through-thickness averaged second-order fiber orientation tensor $\bar{\boldsymbol{A}}$ rendered as superquadric glyphs [34]. Since the fiber orientation does not vary significantly through the thickness [6,29], averaging across the thickness is reasonable. Furthermore, all averaged tensors exhibit strong alignment and pronounced planar orientation, i.e., $\bar{A}_{3i} \approx 0$, $i = 1..3$. Analogous to the flow front, the averaged fiber orientation tensors exhibit rotation around the out-of-plane 3-axis, predominantly in the positive direction. Both the magnitude and sign of this rotation are non-uniform across the plate, which is to be expected given the flow pattern (cf. Fig. 1) and the process-inherent scattering [5]. During the final stages of compression, when the flow front contacts the rear mold wall, significant lateral flow is induced in both the positive and negative 2-direction, causing fibers to rotate strongly around the out-of-plane axis depending on their spatial position within the flow field. This is evident in the top and bottom right glyphs in Fig. 2. Under ideal (symmetric) molding conditions, the resulting fiber orientation of the center-right sample in Fig. 2 would be expected to align predominantly with the 1-direction. The observed deviations from this ideal orientation pattern (cf. Fig. 1), combined with the spatial variability evident in Fig. 2, underscore the material's complex nature.

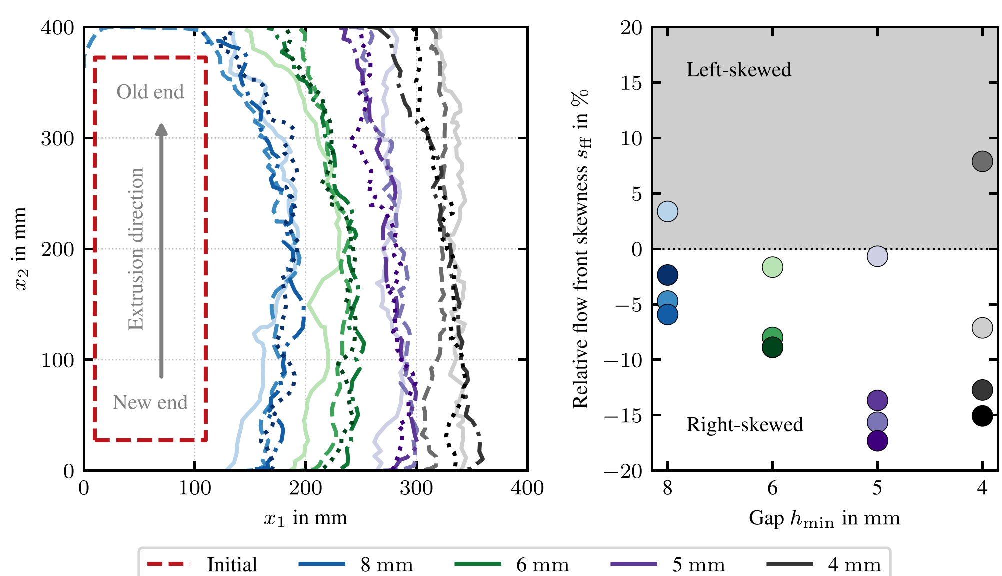

Fig. 1. Experimental flow front contour of individual short shots (line style) for different final tool gaps $h_{\min}$ (color) (left) and relative flow front skewness s_{ff} following [27] (right). Note that each short shot produces exactly one contour, i.e., one line-style–color combination. The red dashed outline in the left subplot indicates the plastificate position at the onset of molding.

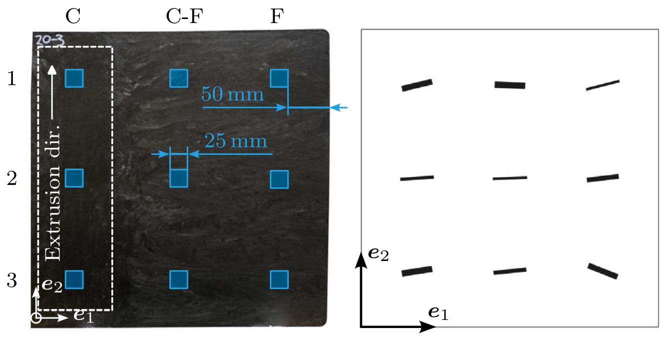

Fig. 2. Location (left) and through-thickness averaged fiber orientation tensor glyphs [34] (right) from µCT scans of a CF-PA6 plate [6]. The samples have dimensions 25 mm × 25 mm × 3 mm. The placement of the plastificate is indicated by the dashed outline on the left. The sample labels follow the nomenclature of [6], where "C" denotes the charge (initial plastificate region), "F" the flow, and "C-F" the intermediate region. The numbers 1, 2, 3 indicate the samples in the 2-direction.

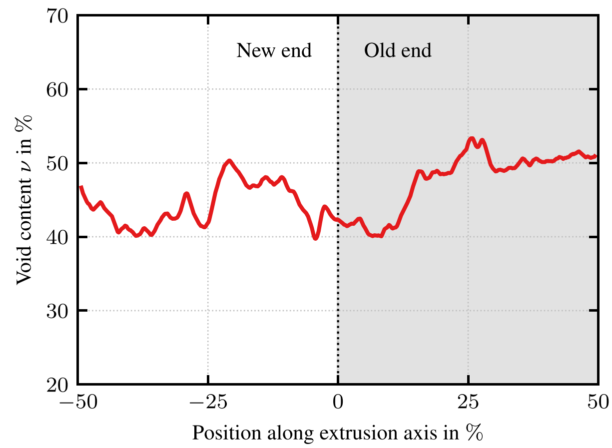

Fig. 3. Void content along the extrusion axis for the GF-PA6 plastificate.

2.2. Plastificate's void content

Voids in the LFT-D plastificate are suspected to originate from the fibrous network that forms as fibers touch and interact during compounding in the second extruder. Upon exiting the second extruder's nozzle, the elastic energy stored within the compressed fibrous network is released, and this spring-back effect is considered the primary driver of void formation. Given the size of the voids (cf. Fig. 4(a), discussed in Section 2.3), it is rather unlikely that the fiber–matrix interface governs void formation.

Since µCT scans of a CF-PA6 plastificate were not available, the void-content analysis is performed using existing µCT data of a GF-PA6 plastificate (with the ends cut off) from [29]. The GF-PA6 features the same PA6 matrix material as the CF-PA6 investigated here, and the scan resolution is 78 µm vx^{-1}. Given that a skewed flow front is observed for both materials (GF-PA6: [27]; CF-PA6: Section 2.1), the void-content characteristics are expected to be qualitatively transferable between the two systems. Fiber volume content, fiber length distribution, fiber curvature, and fiber stiffness may also influence the void-content distribution; however, their influence has not yet been investigated in the literature.

The plastificate's contour along the extrusion axis is determined by a series of morphological operations using circular kernels of size k from the µCT data, as proposed in [29]. The slice-wise void content ν is then determined from the number of void voxels within the detected LFT-D contour (via thresholding) divided by the total number of voxels within the contour. The kernel sizes were chosen as $k_\mathrm{d} = 30$ px for dilation and $k_\mathrm{e} = 15$ px for erosion. An active contour algorithm [35] was also evaluated but proved unable to satisfactorily capture the plastificate's non-convex, irregular contour.

Fig. 3 shows the void-content distribution of the plastificate along the extrusion axis. The void content does not increase continuously along the extrusion direction, but rather exhibits a recurring periodic fluctuation, with the maxima becoming progressively larger towards the old end. These increasing maxima could be attributed to time-dependent lofting effects: because in-line compounding is a continuous extrusion process, a systematic time-after-extrusion gradient exists along the plastificate, with the old end having been exposed to ambient conditions for longer than the new end, leading to more extensive lofting and thus higher void content towards the old end. This interpretation is supported by Schelleis et al. [27], who reported a decrease in the plastificate's effective density of approximately 10 % towards the old end, corresponding to higher void content. Quantitatively, the average void content $\bar{\nu}$ is approximately three percent higher in the old end compared to the new end. Consequently, the measured difference in effective density in [27] is not reflected to the same extent in the void content of the analyzed plastificate. It should be noted that the void-content analysis does not account for local changes in fiber volume content. However, a systematic deviation along the extrusion axis is unlikely given the continuous compounding process. We recognize that utilizing data from a single scan is an approximation; however, it offers an improvement over the current purely qualitative method introduced in [27].

2.3. Plastificate's initial fiber orientation

The fiber orientation distribution within the plastificate is investigated using volume-averaged second-order fiber orientation tensor data determined from µCT scans of cut-outs from CF-PA6 plastificates [23,29]. The scan resolution is approximately 73 µm vx^{-1}, which is several times the diameter of a carbon fiber (≈7.2 µm) due to the large scanned volume. However, Perez et al. [24] demonstrated that fiber bundles reasonably capture the spatial fiber orientation distribution, an assumption successfully adopted in subsequent studies on GF-PP [20] and CF-PA6 [21]. Due to the similar molecular structure of CF and the polymer matrix, the resulting µCT images exhibit low contrast, making algorithmic identification of individual (split) CF bundles challenging. Therefore, the fiber orientation distribution is assumed to follow the structural orientation discernible in the µCT images, which is reasonable given the high void content (cf. Fig. 4a). While higher scan resolutions would enable more precise determination of individual fiber bundles and fibers, the marginal gain in information does not justify the additional scanning and processing effort due to the process-inherent scattering of LFT-D manufacturing. Specifically, fiber orientation at a given location within the plastificate may vary along the extrusion direction (particularly for smaller evaluation volumes); however, the general orientation trends remain consistent due to the continuous nature of the compounding process. A comprehensive discussion of scan properties and sample size for the investigated CF-PA6 is provided in [29]. Given the continuous compounding process within the second twin screw extruder, periodicity in the fiber orientation along the extrusion direction can be assumed [20]. Furthermore, due to the expected twofold symmetry [24], only one quarter of the plastificate and the volume around one extruder screw are evaluated (cf. Fig. 4a). The investigated scan volume was divided into 10 mm × 10 mm × 10 mm cells, from which the fiber orientation is determined. As the fiber orientation in the region of the extruder screw is expected to exhibit higher spatial variation, an additional finer grid of 3.3 mm × 3.3 mm × 3.3 mm was used for this region. The resulting volume-averaged second-order fiber orientation tensors, rendered as superquadric glyphs [34], are shown

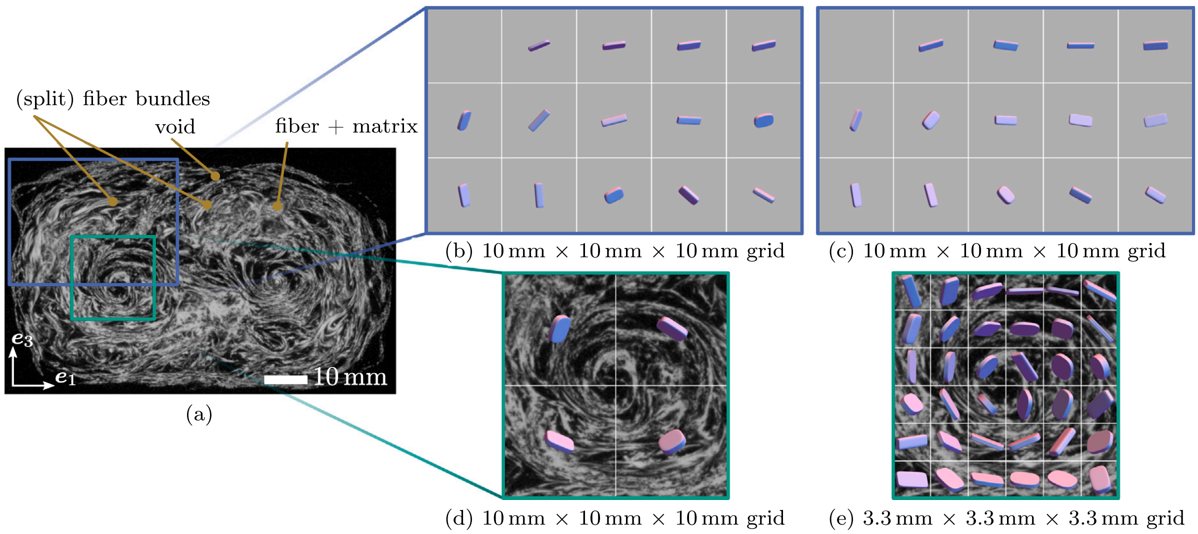

Fig. 4. Volume-averaged second-order fiber orientation tensors $\bar{\boldsymbol{A}}$ rendered as superquadric glyphs [34] of a CF-PA6 plastificate evaluated in (b–c) the upper left quadrant at different positions in extrusion direction and (d–e) around the swirl region where one of the extruder screws was located for different grids. The positions are indicated in the rendered μCT slice shown in (a), which corresponds to the region analyzed in (d–e). The coordinate system in (a) corresponds to the plate coordinate system introduced in Fig. 2.
Source: Adapted from [23,29].

in Fig. 4b–e. Fig. 4b–c show the fiber orientation of one plastificate quarter determined at two separate positions along the extrusion axis, while Fig. 4d–e show the fiber orientation in the volume where the extruder screw was located. In Fig. 4b–c, the upper left volume contains insufficient material for a confident fiber orientation determination. As mentioned in Section 1.1, the fiber orientation tensors exhibit a swirl-like pattern around the extruder screw region (cf. Fig. 4e) and are oriented circumferentially towards the plastificate's contour (cf. Fig. 4b–c). As the available μCT data does not cover the entire plastificate volume, a fiber orientation generation methodology [23] is employed to account for the initial fiber orientation state in the process simulation (cf. Section 3.4).

3. Modeling

This section describes the numerical modeling framework employed to simulate LFT-D compression molding, with a focus on capturing the key phenomena observed experimentally: the formation of skewed flow fronts and spatially varying fiber orientation evolution. First, the governing balance equations and the simulation framework are introduced (Section 3.1). Then, the anisotropic viscous constitutive model and its parameterization are presented, including the fiber orientation evolution equation (Section 3.2). To account for the experimental observations, we describe the incorporation of the initial void-content distribution (Section 3.3) and the geometry-based generation of the three-dimensional initial fiber orientation field (Section 3.4). Finally, the compression molding simulation model is detailed (Section 3.5).

3.1. Governing equations

The motion of the material on a domain Ω is governed by the conservation of mass and linear momentum:

$$\frac{\partial \rho}{\partial t} + \nabla \cdot (\rho \boldsymbol{u}) = 0, \tag{2}$$

$$\frac{\partial (\rho \boldsymbol{u})}{\partial t} + \nabla \cdot ((\rho \boldsymbol{u}) \otimes \boldsymbol{u}) = \nabla \cdot \boldsymbol{\sigma}, \tag{3}$$

where ρ describes the mass density, $\boldsymbol{u}$ the velocity, and $\boldsymbol{\sigma}$ the Cauchy stress tensor. Gravitational forces are neglected as their contribution to the flow dynamics is expected to be negligible. The governing equations are solved on the macroscale using the coupled Eulerian-Lagrangian (CEL) approach [36,37] available in Abaqus/Explicit. In this operator-split framework, the conservation equations are first solved in a Lagrangian step on a deforming mesh, considering only source terms. Subsequently, the solution variables are advected back onto the undeformed mesh using a second-order transport algorithm [36]. To obtain a closed set of equations, an equation of state relating the hydrostatic pressure $p = f(\rho)$ to the density is required.

The material is tracked via the volume-of-fluid method, wherein each element is assigned an Eulerian volume fraction $\alpha \in [0,1]$ representing the material presence. Elements without material have zero volume fraction. The material surface, reconstructed from α, can interact with Lagrangian bodies via contact constraints or form a free surface.

3.2. Anisotropic viscous material model and parameterization

The total stress is split into a spherical and a deviatoric part:

$$\boldsymbol{\sigma} = -p\boldsymbol{I} + \boldsymbol{\tau}, \tag{4}$$

where p denotes the hydrostatic pressure and $\boldsymbol{\tau}$ the viscous stress. The viscous stress is governed by a fourth-order anisotropic viscosity tensor $\mathbb{V}$ that relates the deviatoric rate of strain tensor $\boldsymbol{D}' = \mathbb{I}^{\mathrm{dev}}[\boldsymbol{D}]$ to the viscous stress:

$$\boldsymbol{\tau} = \mathbb{V}' \left[\boldsymbol{D}'\right], \tag{5}$$

with $\mathbb{V}' = \mathbb{I}^{\mathrm{dev}}\, \mathbb{V}\, \mathbb{I}^{\mathrm{dev}}$.

Analogous to our previous work [5], we employ the deviatoric formulation of the orientation-averaged anisotropic viscosity tensor proposed in [15], which depends on the fourth-order fiber orientation tensor $\mathbb{A}$ and the viscous anisotropy ratio R_η:

$$\mathbb{V}' = 2\eta_{23} \left(\mathbb{I}^{\mathrm{dev}} + 2\left(R_\eta - 1\right) \left(\mathbb{A} - \frac{1}{3} (\boldsymbol{I} \otimes \boldsymbol{A} + \boldsymbol{A} \otimes \boldsymbol{I}) + \frac{1}{9} (\boldsymbol{I} \otimes \boldsymbol{I}) \right) \right), \tag{6}$$

where η_{23} denotes the transverse shear viscosity, and $R_\eta = \left(\eta_{11}/\eta_{23} + 1\right)/4$, with η_{11} being the elongational viscosity in fiber direction. Since $\boldsymbol{D}'$ is already deviatoric, only the first index pair of $\mathbb{V}$ must be constrained to the deviatoric space to ensure a purely

Table 1
Isothermal anisotropic viscous material properties of CF-PA6 LFT-D at 255 °C.
Source: Adapted from [5].

Property	Value
Zero-shear-rate viscosity η_0 in MPa s	11.80
Transition shear rate $\dot{\gamma}_0$ in s^{-1}	$4.56 \cdot 10^{-3}$
Power law index n	0.21
Anisotropy ratio R_η	2.20

deviatoric viscous stress. Thus, a computationally efficient reduced form of $\mathbb{V}$ is obtained [38]:

$$\mathbb{V}^{\mathrm{r}} = \mathbb{I}^{\mathrm{dev}}\mathbb{V} = 2\eta_{23}\left(\mathbb{I}^{\mathrm{dev}} + 2\left(R_\eta - 1\right)\left(\mathbb{A} - \frac{1}{3}\left(\boldsymbol{I} \otimes \boldsymbol{A}\right)\right)\right), \tag{7}$$

which satisfies $\boldsymbol{\tau} = \mathbb{V}^{\mathrm{r}}\left[\boldsymbol{D}'\right] = \mathbb{V}'\left[\boldsymbol{D}'\right]$. This reduced formulation eliminates redundant tensor operations compared to Eq. (6), thereby improving computational efficiency.

The transverse shear viscosity $\eta_{23}(\dot{\gamma})$ depends on the shear rate $\dot{\gamma} = \sqrt{2\boldsymbol{D} \cdot \boldsymbol{D}}$ following a Cross-like formulation [39]:

$$\eta_{23} = \frac{\eta_0}{1 + \left(\frac{\dot{\gamma}}{\dot{\gamma}_0}\right)^{1-n}}, \tag{8}$$

where η_0 denotes the zero-shear-rate viscosity, and $\dot{\gamma}_0$ the transition shear rate. The material parameters are adapted from the viscosity characterization of the same CF-PA6 LFT-D in our previous work [5], in which we performed isothermal squeeze flow tests on cylindrical samples with initially aligned fiber orientation. The test samples were cut from compression-molded plates and are therefore void-free; the porosity of the LFT-D plastificate is instead incorporated geometrically as described in Section 3.3. In contrast to the power law model used in our previous work, which is unbounded at low shear rates, the Cross-like model introduces a finite zero-shear-rate viscosity, thereby improving numerical stability. The respective isothermal material parameters at 255 °C, including the viscous anisotropy ratio $R_\eta = 2.2$ [5], are listed in Table 1.

To obtain a closed set of equations (cf. Eqs. (2) and (3)), the hydrostatic pressure $p(\rho)$ is related to the density via a Mie–Grüneisen-like equation of state:

$$p = \rho_0 c_0^2 \left(1 - \frac{\rho_0}{\rho}\right), \tag{9}$$

where ρ_0 denotes the reference density and c_0 the sonic speed.

The evolution of fiber orientation is modeled using the Mori–Tanaka [40] based differential equation, as formulated by Favaloro [41] and generalized by Karl and Böhlke [42]. Including isotropic rotary diffusion [33,43], the evolution equation reads:

$$\begin{aligned}\frac{\mathrm{D}\boldsymbol{A}}{\mathrm{D}t} = {} & \boldsymbol{W}\boldsymbol{A} - \boldsymbol{A}\boldsymbol{W} + \frac{\mu}{\left(1-\varphi_{\mathrm{f}}\right)}\left(\boldsymbol{D}\boldsymbol{A} + \boldsymbol{A}\boldsymbol{D} - 2\mathbb{A}\left[\boldsymbol{D}\right]\right) \\ & + \frac{\varphi_{\mathrm{f}}\mu}{\left(1-\varphi_{\mathrm{f}}\right)}\left(\boldsymbol{D}\boldsymbol{A}\boldsymbol{A} + \boldsymbol{A}\boldsymbol{A}\boldsymbol{D} - 2\boldsymbol{A}\boldsymbol{D}\boldsymbol{A}\right) \\ & + 2C_{\mathrm{i}}\dot{\gamma}\left(\boldsymbol{I} - 3\boldsymbol{A}\right),\end{aligned} \tag{10}$$

where $\boldsymbol{W}$ is the spin tensor, C_{i} is the empirical interaction coefficient, and μ is a shape factor depending on the fiber aspect ratio r_{f}. For slender fibers with $r_{\mathrm{f}} \gg 1$, we set $\mu \approx 1$. The interaction coefficient $C_{\mathrm{i}} = 0.01$ accounts for (random) fiber–fiber interactions that limit the degree of alignment achievable during flow (cf. Fig. 2). In contrast to Jeffery's equation [44] for a single fiber ($\varphi_{\mathrm{f}} \to 0$), the Mori–Tanaka equation accounts for the mean orientation-dependent spin of the fibers through the additional volume-fraction-dependent term in Eq. (10). The required fourth-order orientation tensor $\mathbb{A}$ is approximated from $\boldsymbol{A}$ using the invariant-based optimal fitting (IBOF) closure [45]

$$\mathbb{A} \approx \mathbb{A}^{\mathrm{IBOF}}(\boldsymbol{A}), \tag{11}$$

which preserves orthotropy.

The constitutive equation, fiber orientation evolution equation, and IBOF closure are implemented within a VUMAT user subroutine with five independent state variables for the components of $\boldsymbol{A}$.

3.3. Initial void-content distribution

The plastificate exhibits a substantial void content, including fluctuations along the extrusion axis (cf. Fig. 3). While incorporating the void content through a constitutive material model would be desirable, the continuous nature of the in-line process makes experimental characterization of the compaction behavior challenging. The effective compaction behavior of the whole plastificate could be determined from compression trials with 100 % initial mold coverage, as demonstrated by Meyer et al. [46] for sheet molding compounds (SMC). However, such an approach yields only the average compaction behavior and does not capture the spatial variations in void content along the extrusion direction. Since our primary interest lies in understanding whether these void-content fluctuations contribute to the formation of an inclined flow front, we adopt a geometric approach to incorporate the measured void-content distribution (cf. Fig. 3) into the simulation model.

This geometric approach is based on the assumption that the majority of entrapped air escapes prior to significant flow development. This is supported by the molding experiments, in which a significant press force buildup is delayed until the mold gap falls below approximately 15 mm, which is well below the initial plastificate height of approximately 50 mm. This indicates that the early compression phase is dominated by void collapse rather than lateral material flow. Under this assumption, the LFT-D plastificate can be treated as having uniform material density after void collapse, with the influence of spatially varying void content manifesting solely as a variation in plastificate height. Regions with lower void content therefore retain a greater material height after collapse and provide more material for lateral displacement, causing flow to commence there first. We further consider the most conservative case in which lofting occurs exclusively in the height direction (3-direction in Fig. 2), i.e., the plastificate exhibits no geometric skewness in plan view at the onset of molding. The observed flow front asymmetry thus develops progressively during compression, consistent with experimental observations.

The methodology begins with an idealized plastificate geometry (rectangular cuboid) whose dimensions correspond to the average ones of the physical plastificate. The plastificate height $h(x_2)$ along the extrusion direction x_2 is then scaled by the solid fraction $\left(1 - v(x_2)\right)$, derived from the experimentally determined void-content distribution $v(x_2)$ from Fig. 3, as illustrated in Fig. 5. To obtain a smoother height profile, the discrete void-content measurements are approximated by a higher-order polynomial. Given that the void-content analysis is performed on GF rather than CF plastificates (due to data unavailability) and that the virtual plastificate's geometry is idealized (rectangular cuboid), the plastificate height is uniformly scaled so that its volume slightly exceeds the final part volume, thereby avoiding short shots and favoring slight overfill in the simulation.

3.4. Initial fiber orientation state

As demonstrated in Section 2.3, the LFT-D plastificate exhibits a spatially varying initial fiber orientation distribution. To account for this in the simulation, we employ the geometry-based fiber orientation generation approach introduced in [23], which creates a realization of the plastificate's initial fiber orientation that reproduces the characteristic features observed in physical plastificates. This geometric approach enables consideration of the initial fiber orientation without requiring (high-resolution and full-field) μCT scans and subsequent postprocessing. However, μCT scans were used to initially identify and characterize the features of the initial fiber orientation field [23].

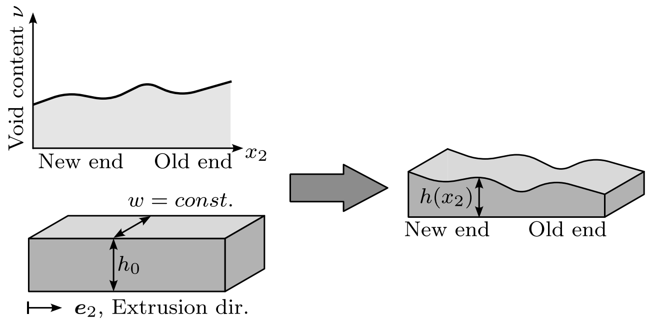

Fig. 5. Schematic of geometry-based void-content modeling.

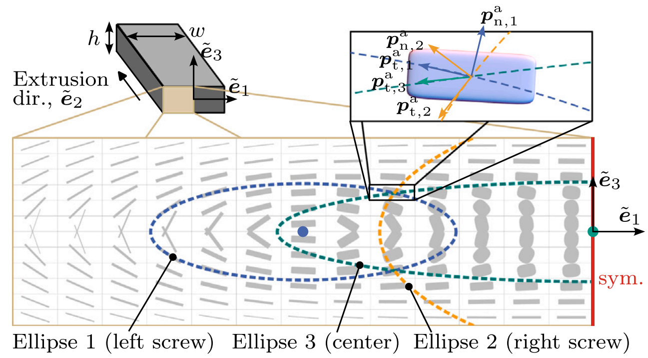

Fig. 6. Glyphs of the initial fiber orientation $A_0(x)$ generated from artificial fibers p^a following [23] on an exemplary grid.

The fiber-orientation generation methodology constructs artificial fiber orientations $p^a \in \mathcal{S}^2$ from the tangent and normal vectors of ellipses with centers at the positions of the extruder screws' centers and at the center of the plastificate's cross-section perpendicular to the extrusion direction, as illustrated in Fig. 6. The numeric indices $(\cdot)_j$, with $j = 1, 2, 3$, in Fig. 6 denote the ellipses, and $(\cdot)_t$ and $(\cdot)_n$ denote whether the fiber is constructed from the tangent or the normal of the ellipse. The ellipse axis ratios (horizontal divided by vertical axis) are set to $w/(2h)$ and w/h for the ellipses at the extruder screws (indices 1 and 2) and the cross-section center (index 3), respectively, depending on the plastificate's width w and height $h(x_2)$. The element-wise second-order fiber orientation tensor $A_0(\tilde{x})$ with respect to the local plastificate coordinate system $\{\tilde{e}_i\}$ (cf. Fig. 6), is then computed as the weighted sum of the five discrete artificial fiber orientations p^a_i (cf. Fig. 6):

$$A_0(\tilde{x}) = \frac{1}{\sum_i^5 \omega_i(\tilde{x})} \sum_i^5 \omega_i(\tilde{x}) p^a_i(\tilde{x})^{\otimes 2}, \tag{12}$$

where $\omega_i(\tilde{x})$ denotes the weight function of the ith fiber vector. The weight functions for the fiber orientations constructed from the tangents are defined as

$$\omega_{t,1} = \frac{d_1 + d_2}{d_1}, \tag{13}$$

$$\omega_{t,2} = \frac{d_1 + d_2}{d_2}, \tag{14}$$

$$\omega_{t,3} = \begin{cases} \omega_{t,1} \operatorname{argmax}\left(\frac{2|\tilde{x}_3|}{h}, \frac{2|\tilde{x}_1|}{w}\right)^4, & \tilde{x}_1 \le 0 \\ \omega_{t,2} \operatorname{argmax}\left(\frac{2|\tilde{x}_3|}{h}, \frac{2|\tilde{x}_1|}{w}\right)^4, & \tilde{x}_1 > 0, \end{cases} \tag{15}$$

and for the fiber orientations constructed from the normals (only for fibers from extruder screw ellipses) as

$$\omega_{n,j} = \omega_{t,j} \operatorname{argmin}\left(1 - \frac{2|\tilde{x}_3|}{h}, 1 - \frac{2|\tilde{x}_1|}{h}\right)^2, \quad j = 1, 2, \tag{16}$$

where d_1 and d_2 denote the Euclidean distances between the material point and the respective ellipse centers. The artificial fiber orientation field is constructed to lie within the plane perpendicular to the extrusion direction (1,3-plane in the local plastificate coordinate system). The out-of-plane component A_{22} (in extrusion direction) is assigned a constant value of 0.1, consistent with the experimentally determined predominantly planar fiber orientation states shown in Fig. 4, which also aligns with observations in [29] on GF-PA6 featuring the same PA6 matrix. As evident from Fig. 6, the generated orientation field reproduces the characteristic features observed in the physical plastificate (cf. Fig. 4): circumferential orientation at the perimeter, swirl-like patterns around the extruder screw positions, and more isotropic orientation towards the center. The thin surface layer exhibiting strong alignment in the extrusion direction is not explicitly modeled, as its influence on flow behavior is negligible. Furthermore, accurately capturing this boundary layer would necessitate very fine mesh discretization near the plastificate's surface; otherwise, its contribution would be artificially overestimated. The plastificate's fiber orientation field is mapped onto the Eulerian simulation mesh using Euclidean interpolation [47] with inverse distance weighting [48].

3.5. Compression molding simulation model

The mold cavity is represented by an Eulerian mesh using hexahedron elements with reduced integration (EC3D8R). The LFT-D plastificate is defined as an initially filled subset through an element volume fraction field α. The plastificate's height distribution $h(x_2)$ along the extrusion direction is prescribed according to the procedure in Fig. 5 and the void-content distribution in Fig. 3. The corresponding maximum and minimum plastificate heights are about 16.8 mm and 14.0 mm, respectively. As illustrated in Fig. 7, we exploit symmetry with respect to the 1,2-plane and model only the upper half of the cavity. Since thermal effects are not considered, we use a constant temperature of 255 °C. The mold is modeled as a rigid body (shell elements: R3D4). The rigid body interacts with the LFT-D surface via a penalty-based contact formulation that prevents penetration in the normal direction and enforces a no-slip boundary condition in the tangential direction. The latter is the standard boundary condition for thermoplastic-based molding composites, as a solidified thermoplastic layer forms at the mold surface due to rapid heat dissipation into the cold mold. The no-slip condition was experimentally verified by spraying a dot pattern on the plastificate's surface, which remained quasi-unsmeared after molding. The compression speed $\dot{h}(h)$ is prescribed via compression-speed-mold-gap tuples in the VUAMP subroutine as in [39]. A schematic of the initial setup including the boundary conditions, model dimensions, and the plastificate's extrusion direction is shown in Fig. 7.

To increase the computational efficiency of the explicit time integration scheme, a global mass scaling of 10^4 is applied. The validity of this scaling is ensured by verifying that the kinetic energy remains sufficiently small compared to the total work throughout the simulation. The time increment is additionally scaled by a constant factor of 0.7 to increase numerical stability in the presence of contact interactions and material nonlinearities.

4. Numerical investigation

In this section, we numerically investigate the compression molding process using the simulation model described in Section 3.5. The analysis is structured in two parts: First, we examine the influence of mesh discretization on the predicted flow front evolution and resulting fiber orientation field. Then, we investigate the sensitivity of the fiber orientation evolution to the viscous anisotropy ratio R_η. Throughout these studies, particular attention is given to the formation of the skewed flow front observed experimentally (cf. Fig. 1) and its relationship to the initial void-content distribution and fiber orientation field. Unless otherwise specified, the material parameters listed in Table 1 are used.

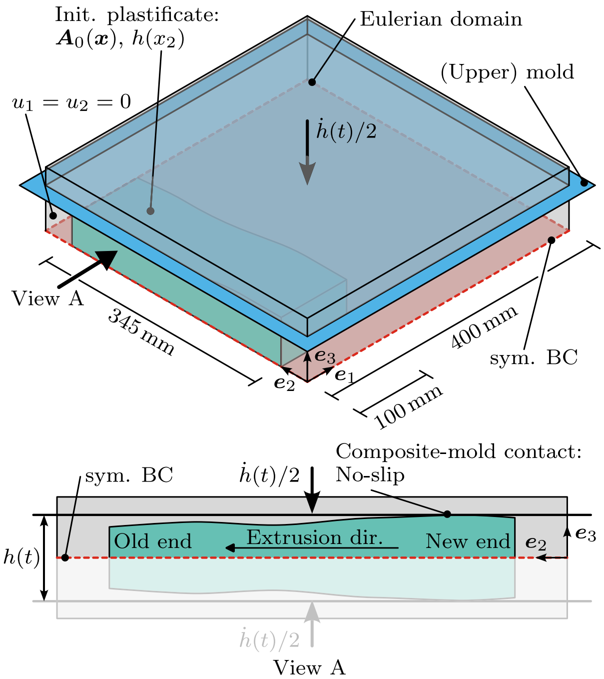

Fig. 7. Schematic of the (symmetric) simulation model at the onset of molding with lateral view (View A) at the bottom. The extrusion direction is indicated in View A.

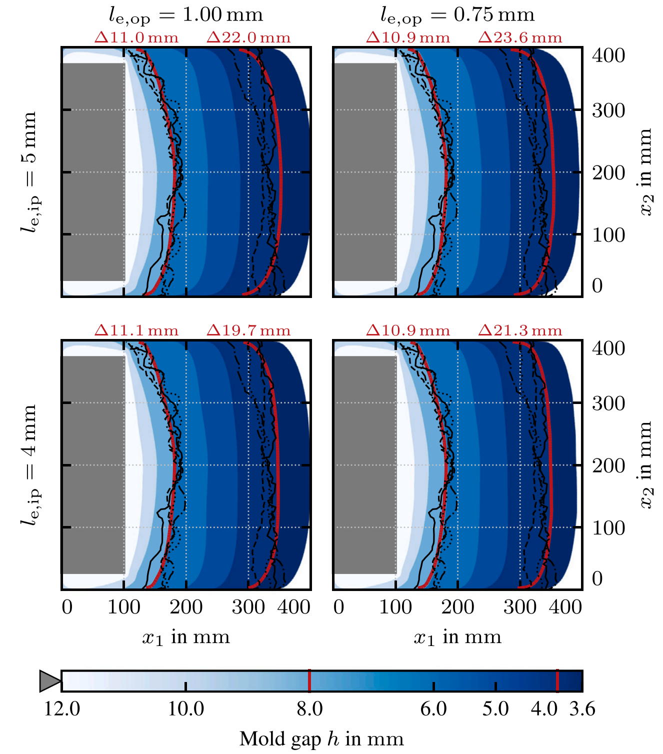

Fig. 8. Flow front evolution for different in-plane and out-of-plane element lengths $l_{\mathrm{e,ip}}$, $l_{\mathrm{e,op}}$. The flow front is reconstructed at $\alpha = 0.5$, and the gray block corresponds to the initial contour. For reference, the experimental contours at eight and four millimeters are included (black lines), and the corresponding simulated contours are highlighted in red. The root mean square errors (RMSE) between experimental and simulated contours at these mold gaps are annotated in red.

4.1. Mesh size influence

For the mesh study, we simulated the numerical model described in Section 3.5 with different in-plane (ip; 1,2-plane in Fig. 7) and out-of-plane (op; 3-direction) element lengths: $l_{\mathrm{e,ip}} \in \{4, 5\}$ mm and $l_{\mathrm{e,op}} \in \{0.75, 1.00\}$ mm. In the out-of-plane direction, the mesh begins with two uniform elements of height $l_{\mathrm{e,op}}$ at the symmetry plane ($x_3 = 0$). Beyond these, a linear bias is applied, with element heights increasing progressively to approximately 2.0 mm at the top of the Eulerian domain, resulting in a total domain height of approximately 18.5 mm. The explicit time integration scheme in Abaqus/Explicit constrains through-thickness mesh discretization due to computational cost. The stable time increment scales directly with element size, and material anisotropy ($R_\eta > 1.0$) further reduces this increment due to directional variations in viscous response. At the onset of molding, sufficient through-thickness elements are available to capture the three-dimensional fiber orientation. Towards the end of flow, when fiber orientation becomes predominantly planar, the predicted flow field and fiber reorientation represent approximations of the actual through-thickness behavior. Nevertheless, Blarr [29] demonstrated for both CF-PA6 (identical material) and GF-PA6 (identical PA6 matrix) that the resulting fiber orientation exhibits minimal through-thickness variation. This is attributed to the progressively narrowing mold gap during compression, which geometrically constrains out-of-plane fiber rotation, resulting in predominantly planar fiber alignment at the end of molding.

Fig. 8 shows the predicted flow patterns for the different discretizations. The numerical flow front is reconstructed as an isosurface at $\alpha = 0.5$, and the gray box indicates the initial plastificate position. The experimental flow front contours (black lines; cf. Fig. 1) and the corresponding simulated contours (red lines) at mold gaps of eight and four millimeters are added for reference. The root mean square errors (RMSE) between the experimental and simulated contours at these mold gaps are annotated in red. All simulations exhibit the formation of a skewed flow front arising from the prescribed void-content distribution, which becomes particularly pronounced towards the end of molding. Neither in-plane nor out-of-plane discretization significantly affects the predicted flow pattern. The simulated contours are in good agreement with the experimental contours at a gap of eight millimeters, supporting the validity of the geometric modeling approach and suggesting that the inhomogeneous void-content distribution is adequately captured. Additionally, the predicted fiber orientation field is compared against the experiments.

Fig. 9 shows glyphs of the through-thickness averaged second-order fiber orientation tensors $\bar{\boldsymbol{A}}$ at the experimental sample positions from both simulation (dark gray) and experiment (light gray). The coloring represents the principal fiber direction ϑ (predicted by the simulation), defined as the angle about $\boldsymbol{e}_3$ (cf. Fig. 7) formed by the eigenvector corresponding to the largest eigenvalue of $\bar{\boldsymbol{A}}$. Since eigenvectors have no preferred direction, angles are mapped to the range $\vartheta \in (-90\,°, +90\,°]$. The predicted fiber orientation fields are similar across all mesh discretizations (cf. Fig. 9). As expected, the skewed flow front is reflected in the resulting fiber orientation tensor field $\bar{\boldsymbol{A}}(\boldsymbol{x})$, which exhibits significant spatial variation. In contrast to a simulation with uniform plastificate height (i.e., without void-content distribution; cf. Appendix A), the fiber orientation field lacks symmetry with respect to the 1, 3-plane at half mold width ($x_2 = 200$ mm). Instead, a distinct rotation about the out-of-plane 3-axis in positive 2-direction is observed across this plane (see glyphs at $x_2 = 200$ mm in Fig. 9). The pronounced rotation about the out-of-plane axis towards the corners in the flow region ($x_1 > 300$ mm) results from flow deflection when the material makes contact with the rear mold wall.

Comparing predictions with experiments reveals good agreement at most sample positions (signed angular deviations are listed in Appendix B). At the top right and bottom right positions, the predicted fiber

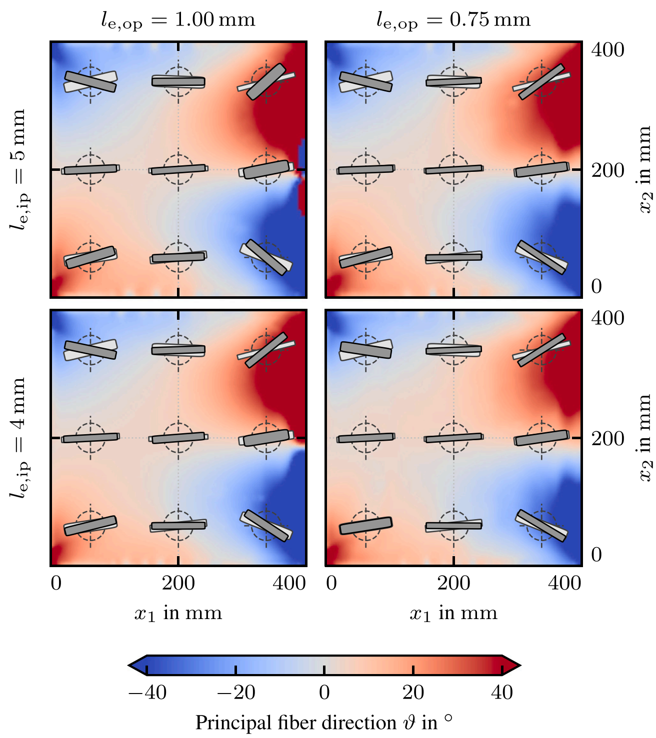

Fig. 9. Glyphs and principal fiber direction ϑ of $\bar{\boldsymbol{A}}$ at the end of compression for different in-plane and out-of-plane element lengths $l_{e,ip}$ and $l_{e,op}$. Experimental fiber orientation glyphs are included for reference (light gray). The principal fiber direction is defined as the angle about $\boldsymbol{e}_3$ formed by the eigenvector corresponding to the largest eigenvalue of $\bar{\boldsymbol{A}}$. Since eigenvectors have no preferred direction, angles are mapped to the range $(-90°, +90°]$.

orientation tensor exhibits the same sense of rotation about $\boldsymbol{e}_3$ as observed experimentally, though the rotation amplitude differs from the experiments. At the top left position, however, the predicted rotation direction does not match the experimental observation, whereas the predicted fiber orientation by the simulation is plausible given the flow pattern (cf. Fig. 8). In addition to rotational dependency about $\boldsymbol{e}_3$, the shape of the fiber orientation tensors also exhibits slight mesh dependency. The shape is evaluated based on the fractional anisotropy $FA = \sqrt{3/2}\|\boldsymbol{A}'\|/\|\boldsymbol{A}\|$, where $\boldsymbol{A}' = \boldsymbol{A} - \boldsymbol{I}/3$ denotes the deviatoric part of $\boldsymbol{A}$, and $\|\cdot\|$ denotes the Frobenius norm. The FA is a measure for the degree of fiber alignment. The finest discretization (cf. bottom right in Fig. 9) predicts higher FA than the coarsest (cf. top left), though both show good agreement with the experiments, with the finer mesh matching slightly better. Accordingly, for the subsequent investigation, we adopt the discretization $l_{e,ip} = 4$ mm and $l_{e,op} = 1$ mm as this represents a reasonable compromise between computational efficiency and predictive accuracy.

4.2. *Influence of fiber-induced anisotropy*

To investigate the influence of fiber-induced anisotropy on flow behavior and fiber orientation evolution, simulations with two-way flow–orientation coupling and varying viscous anisotropy ratios $R_\eta = \{2.2, 4.0, 8.0\}$ and one simulation with one-way coupling (isotropic viscosity) are performed. The viscous anisotropy ratio $R_\eta = 2.2$ follows from squeeze flow characterization (cf. Table 1). Fig. 10 presents the evolution of the through-thickness averaged fiber orientation tensor fields $\bar{\boldsymbol{A}}(t, \boldsymbol{x})$ at different mold gaps $h(t)$. Fig. 11 shows the flow patterns.

We deliberately choose the viscous anisotropy ratio $R_\eta = 8$ as the extreme case, in which the Abaqus CEL approach ultimately fails before the desired mold gap is reached. This is due to artificial diffusion of linear momentum and a tendency towards zero energy states, where viscous stress and rate of strain tensor are almost orthogonal. Attempts to stabilize the simulation through finer mesh discretization ($l_{e,op} = 0.75$ mm) resulted in even earlier termination, as the reduced element size further decreased the critical time increment. Consequently, results are presented only up to the mold gap preceding numerical instability. Assuming a monotonic evolution of fiber orientation during molding, the available evolution data still provide valuable insights into the influence of stronger anisotropy coupling on flow development.

For one-way coupling (top row in Fig. 10), the fiber orientation field lacks symmetry with respect to the 1, 3-plane at half mold width ($x_2 = 200$ mm) and exhibits a slight rotation about the out-of-plane 3-axis in this region, which is also reflected in the flow pattern (cf. Fig. 11a). This demonstrates that the inhomogeneous void content alone induces asymmetric flow patterns, independent of anisotropic viscous effects, which aligns with our purely qualitative study in [27]. The fiber orientation evolution for $R_\eta = 2.2$ (second row in Fig. 10) exhibits only subtle differences in both flow pattern and fiber reorientation compared to the isotropic case (one-way coupling). The initially predominantly in-plane fiber alignment in the 1,3-plane promotes material flow in the 2-direction, causing the material to contact the mold wall slightly earlier than in the isotropic case (compare white contours at $h = 12$ mm in Fig. 11a and b). However, once both mold walls are reached, the flow is geometrically constrained to a quasi-one-dimensional state in which anisotropic viscosity has limited capacity to alter the flow direction. With increasing R_η, the flow front becomes more irregular (cf. Fig. 11c–d), and as molding progresses and the mold gap narrows, spatial variations in fiber orientation, specifically in the principal fiber direction ϑ, become more pronounced (compare, e.g., $R_\eta = 2.2$ and $R_\eta = 8$ at $h = 3.6$ mm in Fig. 10). The asymmetric velocity field resulting from the initial void-content distribution drives fiber reorientation through the velocity gradient. Simultaneously, the fiber-orientation-dependent viscous stress generates higher flow resistance in the fiber direction, preferentially directing material flow transverse to the local fiber orientation. This flow deflection further reorients the fibers, establishing a coupling mechanism between fiber orientation and flow direction that is driven by anisotropic viscous behavior.

5. Discussion

Influence of plastificate properties and anisotropy coupling. The simulation results with orientation-independent viscosity already exhibit a skewed flow front, which can solely be attributed to the inhomogeneous void content, thereby corroborating the findings in Schelleis et al. [27]. Since the flow becomes quasi-one-dimensional once the material reaches the upper and lower mold walls, anisotropic coupling effects are largely suppressed by the geometric confinement. Therefore, anisotropic effects are not as pronounced in the simulations with the viscous anisotropy ratio R_η characterized in our previous work [5]. However, with increasing viscous anisotropy ratio R_η, which might be achieved when increasing the fiber volume content or the average fiber length, e.g., by changing the twin screw extruder settings, the evolving fiber orientation exhibits stronger spatial variations, especially in the investigated limiting case of $R_\eta = 8$. The initial fiber orientation field is mainly governed by the screw geometry (cf. Section 2.3) and is assumed to be independent of the lofting mechanism, i.e., $\partial \boldsymbol{A}_0/\partial x_2 = 0$. Therefore, the skewed flow front must follow from the initial void-content distribution. While the geometry-based modeling approach for the void content poses a simplification, experimental characterization of the actual physical behavior is not readily available due to in-line compounding, as discussed in Section 3.3. Nevertheless, assuming an initial collapse of voids, it is to be expected that material flow will begin first in regions with lower void content, which is captured by the simulations.

The void-content distribution used in this study was characterized on a GF-PA6 plastificate (identical PA6 matrix), as µCT data of a CF-PA6

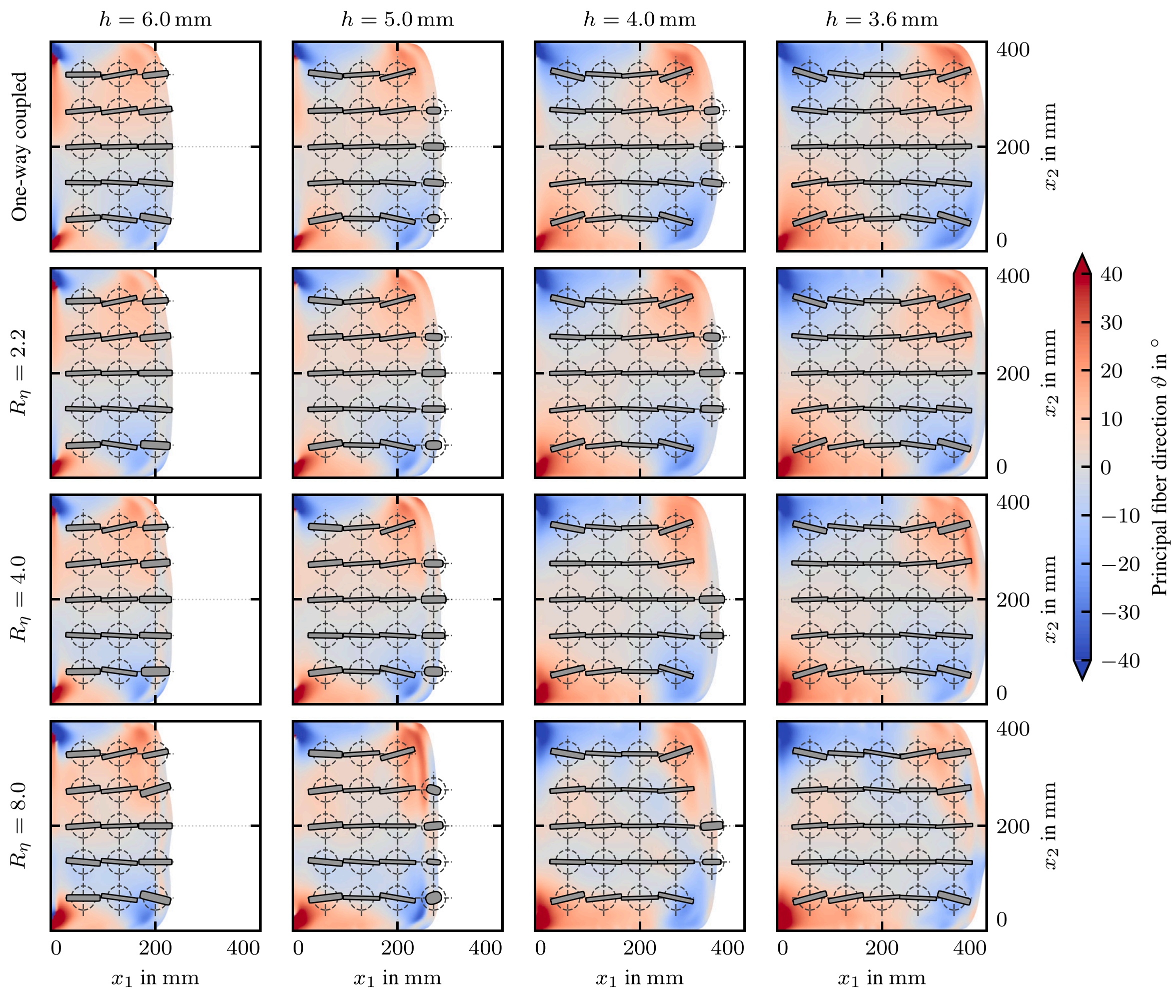

Fig. 10. Evolution of glyphs and principal direction ϑ of $\bar{\boldsymbol{A}}(t, \boldsymbol{x})$ for different anisotropy ratios R_η and one simulation with one-way coupling (isotropic viscosity) at decreasing mold gaps $h(t)$. The flow front is reconstructed at $\alpha = 0.5$. For $R_\eta = 8$, the simulation terminated prematurely; only results preceding numerical instability are shown.

plastificate were not available. Since a skewed flow front is observed for both materials, utilization of the GF-PA6 data is more reasonable than restricting oneself to the purely qualitative approach in [27], where we assumed a trapezoidal shape. Furthermore, the ends of the GF-PA6 plastificate were cut off during sample preparation. Given the free surface at the ends of the plastificate, the void content at the ends is expected to be higher, which has not yet been considered given the data restrictions and should be addressed in future work. In addition, to further increase the accuracy of the simulation, the actual contour of the plastificate could be discretized. Nonetheless, the simulations show that the inhomogeneous plastificate properties at the onset of molding are crucial to accurately predict the flow behavior.

Implications for mechanical characterization. These findings also translate to mechanical characterization, which is typically done on samples from compression molded plates with lateral plastificate positioning to emphasize fiber alignment via the flow path length. In addition to the scatter between plates, the fiber orientation within a plate is also strongly dependent on the position of sample extraction. According to the fiber orientation field predicted by the simulation (cf. Fig. 9), the position and orientation of the samples must be chosen based on the local fiber orientation to minimize scatter in mechanical properties. Therefore, it might not be meaningful to estimate a global average fiber orientation of a plate from sparse fiber orientation data obtained via μCT (cf. Fig. 2) as in [6]. Consequently, process simulations can serve as a valuable tool for guiding sample extraction and improving the reliability of mechanical characterization.

Numerical limitations. Although the fully coupled simulation method captures process-specific effects, several limitations apply. The stable time increment depends strongly on element size and the instantaneous directional viscosity. This severely restricts through-thickness discretization to maintain acceptable computation times, limiting the resolution with which the through-thickness velocity profile can be approximated. A no-slip boundary condition, which is physically plausible for LFT-D (cf. Section 3.5), produces a highly nonlinear through-thickness velocity profile that becomes even steeper when shear-thinning is included. In Abaqus CEL, however, velocity boundary conditions are not explicitly imposed but approximated implicitly via fluid–structure interaction. This, combined with the limited through-thickness resolution, prevents an accurate prediction of compression forces. Fine through-thickness resolution is likewise required to model thermal effects, which are therefore not considered in this work. Moreover, the decreasing mold gap during compression leads to increasing deformation rates and thus a progressively smaller stable time increment. Consequently, the global mass scaling factor must be tuned to the most critical stage of molding — typically near the end of flow where shear rates are highest and fewest through-thickness elements remain

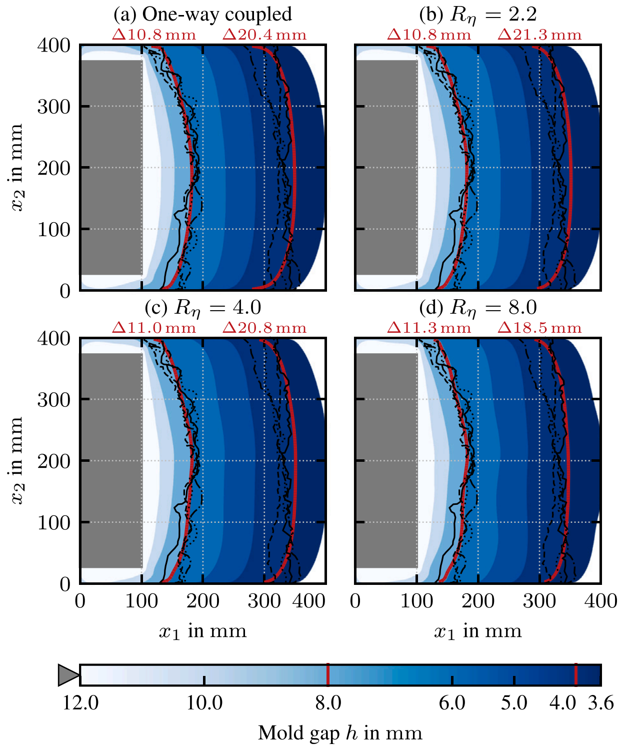

Fig. 11. Numerical flow front evolution for different anisotropy ratios R_η and one simulation with one-way coupling (isotropic viscosity). The flow front is reconstructed at $\alpha = 0.5$. The gray block corresponds to the initial contour. For reference, the experimental contours at eight and four millimeters are included (black lines), and the corresponding simulated contours are highlighted in red. The root mean square errors (RMSE) between experimental and simulated contours at these mold gaps are annotated in red.

— substantially reducing computational efficiency throughout the simulation. To the authors' knowledge, no existing compression molding simulation yet combines a fully anisotropic viscosity model, shear-thinning behavior, and a no-slip boundary condition. Several recent studies [49–51] have employed the informed isotropic (IISO) viscosity model [38] instead of a fully anisotropic viscosity model to leverage robust isotropic compression molding solvers that permit finer through-thickness discretization and thus a no-slip condition. However, we have shown that the IISO model cannot accurately capture anisotropic viscous behavior in compression molding [52] and should therefore be avoided when investigating flow–fiber coupling effects. Therefore, the proposed simulation approach poses a reasonable compromise between physical fidelity and computational feasibility at the current state of the art.

6. Conclusion

This work presented a two-way flow–orientation coupled simulation methodology for LFT-D compression molding that simultaneously accounts for anisotropic viscous behavior, the plastificate's initial fiber orientation, and its spatially varying void content. A geometry-based fiber orientation generation approach was employed to prescribe the plastificate's initial fiber orientation state without requiring full-field μCT scans, reproducing the characteristic features observed in physical plastificates. Furthermore, a geometry-based approach for incorporating the experimentally determined void-content distribution was introduced, wherein the plastificate's height is scaled along the extrusion direction according to μCT-derived void-content data. The simulations demonstrate that this inhomogeneous void-content distribution is the major contributing factor to the formation of the skewed flow front observed experimentally, corroborating the experimental findings in the literature. Already a one-way coupled simulation, i.e., assumed isotropic viscous behavior, exhibits a skewed flow pattern solely due to the prescribed void-content distribution. This underscores the importance of accurately characterizing and modeling the plastificate's initial state. Since the flow is geometrically constrained once the material reaches both mold walls in the investigated plate geometry, the two-way coupled simulation with the experimentally characterized viscous anisotropy ratio yields only subtle differences compared to the one-way coupled case. However, with increasing viscous anisotropy ratio, two-way flow–orientation coupling becomes more relevant, leading to more spatial variations in the fiber orientation field.

Several aspects require further investigation to improve the predictive accuracy. The void-content distribution used in this study was obtained from a GF-PA6 plastificate due to the unavailability of CF-PA6 μCT data. Therefore, we encourage future work to conduct a more extensive end-to-end characterization study. This comprises void-content determination and resulting fiber orientation tensor scans for a significant sample size. Regarding the simulation methodology, the through-thickness discretization is constrained by the critical time increment in the explicit integration scheme, particularly in the presence of anisotropy coupling and no-slip boundary conditions. As a result, the through-thickness velocity gradient is only coarsely resolved towards the end of flow, limiting the framework's applicability to complex three-dimensional parts. Nonetheless, the simulations highlight the importance of accurately modeling the plastificate's initial conditions and confirm that the void-content distribution is a decisive factor governing the flow front evolution during compression molding.

CRediT authorship contribution statement

Louis Schreyer: Writing – review & editing, Writing – original draft, Visualization, Validation, Software, Methodology, Investigation, Formal analysis, Data curation, Conceptualization. **Florian Wittemann:** Writing – review & editing. **Luise Kärger:** Writing – review & editing, Supervision, Project administration, Funding acquisition, Conceptualization.

Declaration of Generative AI and AI-assisted technologies in the writing process

During the preparation of this work the authors used Anthropic Claude Opus and Claude Sonnet in order to improve the readability and language of the manuscript. After using these tools, the authors reviewed and edited the content as needed and take full responsibility for the content of the published article.

Declaration of competing interest

The authors declare that they have no known competing financial interests or personal relationships that could have appeared to influence the work reported in this paper.

Acknowledgments

This research was funded by the German Research Foundation (DFG) through two successive projects: the International Research Training Group "Integrated engineering of continuous-discontinuous long fiber reinforced polymer structures" (IRTG 2078) and the Heisenberg project "Digitalization of fiber-reinforced polymer processes for resource-efficient manufacturing of lightweight components" (455807141). The support by the DFG is gratefully acknowledged. We also gratefully acknowledge Fraunhofer Institute for Chemical Technology in Pfinztal, Germany, in particular Christoph Schelleis, for conducting the flow study.

Appendix A. Two-way coupled simulation with uniform void content

This section presents simulation results obtained without accounting for the void-content distribution, i.e., assuming a uniform void content along the plastificate and, consequently, a constant plastificate height. All other aspects of the model follow Section 3.5, and the material parameters are taken from Table 1. Fig. A.1 shows the flow front evolution, and Fig. A.2 shows the principal fiber direction ϑ and glyphs of the predicted through-thickness averaged fiber orientation tensor field $\bar{\boldsymbol{A}}$. As expected, both the flow front evolution and $\bar{\boldsymbol{A}}$ are symmetric about $x_2 = 200$ mm, i.e., not skewed. Furthermore, the fiber orientation tensors at the symmetry plane ($x_2 = 200$ mm) are aligned along the 1-direction.

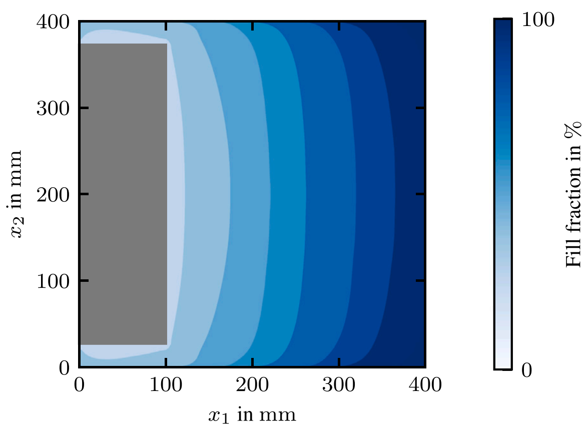

Fig. A.1. Flow front evolution for simulation without consideration of void-content distribution. The flow front is reconstructed at $\alpha = 0.5$, and the gray block corresponds to the initial contour.

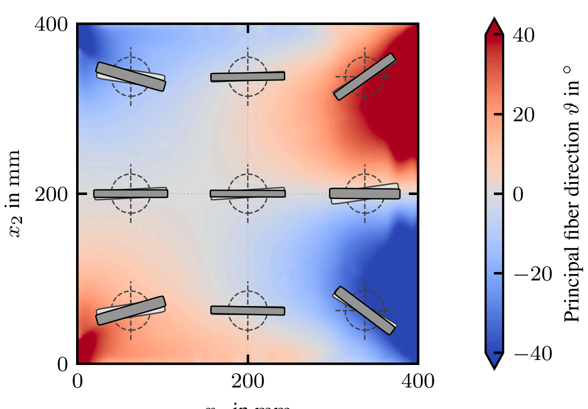

Fig. A.2. Glyphs and principal fiber direction ϑ of $\bar{\boldsymbol{A}}$ at the end of compression for the simulation without consideration of the void-content distribution. For comparison, the fiber orientation glyphs from the simulation accounting for the void-content distribution (cf. Fig. 9, bottom right) are superimposed in light gray.

Appendix B. Quantitative comparison with experiments

Table B.1 lists the signed angular deviation $\Delta\vartheta = \vartheta_{\text{sim}} - \vartheta_{\text{exp}}$ of the principal fiber direction ϑ of $\bar{\boldsymbol{A}}$ between the mesh-study simulations and the experiments for all nine measurement positions (cf. Fig. 2). The graphical comparison via tensor glyphs is shown in Fig. 9.

Table B.1
Signed angular deviation $\Delta\vartheta = \vartheta_{\text{sim}} - \vartheta_{\text{exp}}$ in the principal fiber direction ϑ of $\bar{\boldsymbol{A}}$ between simulations and experiments. The sample nomenclature is defined in Fig. 2.

Position	$\Delta\vartheta$ in °			
	$l_{\text{e,ip}} = 5$ mm		$l_{\text{e,ip}} = 4$ mm	
	$l_{\text{e,op}} = 1.0$ mm	$l_{\text{e,op}} = 0.75$ mm	$l_{\text{e,op}} = 1.0$ mm	$l_{\text{e,op}} = 0.75$ mm
C-1	−28.5	−27.1	−25.5	−22.3
C-2	−1.1	−1.7	−0.8	−0.9
C-3	8.0	6.7	5.3	0.3
C-F-1	2.7	5.0	4.4	4.8
C-F-2	1.78	1.3	2.3	1.6
C-F-3	−3.7	−5.3	−5.5	−6.3
F-1	27.7	22.1	24.3	18.1
F-2	4.6	0.8	2.7	1.7
F-3	−18.5	−12.1	−11.5	−9.4

Data availability

Data will be made available on request.

References

[1] Ning H, Lu N, Hassen AA, Chawla K, Selim M, Pillay S. A review of long fibre thermoplastic (LFT) composites. Int Mater Rev 2020;65:164–88. http://dx.doi.org/10.1080/09506608.2019.1585004.

[2] Chen T, Mansfield CD, Ju L, Baird DG. The influence of mechanical recycling on the properties of thermotropic liquid crystalline polymer and long glass fiber reinforced polypropylene. Compos B 2020;200:108316. http://dx.doi.org/10.1016/j.compositesb.2020.108316.

[3] Krause W, Henning F, Tröster S, Geiger O, Eyerer P. LFT-D — a process technology for large scale production of fiber reinforced thermoplastic components. J Thermoplast Compos Mater 2003;16:289–302. http://dx.doi.org/10.1177/0892705703016004001.

[4] Schelleis C, Scheuring BM, Liebig WV, Hrymak AN, Henning F. Approaching polycarbonate as an LFT-D material: processing and mechanical properties. Polymers 2023;15:2041. http://dx.doi.org/10.3390/polym15092041.

[5] Schreyer L, Krauß C, Scheuring BM, Hrymak A, Kärger L. Characterization and modeling of the anisotropic flow behavior of long carbon fiber reinforced thermoplastic compression molding. Compos A 2025;198:109053. http://dx.doi.org/10.1016/j.compositesa.2025.109053.

[6] Scheuring BM, Christ N, Blarr J, Liebig WV, Hohe J, Montesano J, Weidenmann KA. Experimental and homogenized orientation-dependent properties of hybrid long fiber-reinforced thermoplastics. Int J Mech Sci 2024;280:109470. http://dx.doi.org/10.1016/j.ijmecsci.2024.109470.

[7] Bondy M, Pinter P, Altenhof W. Experimental characterization and modelling of the elastic properties of direct compounded compression molded carbon fibre/polyamide 6 long fibre thermoplastic. Mater Des 2017;122:184–96. http://dx.doi.org/10.1016/j.matdes.2017.03.010.

[8] Ericsson KA, Toll S, Månson J-AE. The two-way interaction between anisotropic flow and fiber orientation in squeeze flow. J Rheol 1997;41:491–511. http://dx.doi.org/10.1122/1.550833.

[9] Dweib MA, Ó Brádaigh CM. Anisotropic modeling of isothermal squeezing flow of glass-mat reinforced thermoplastics (GMT). Polym Compos 1998;19:588–99. http://dx.doi.org/10.1002/pc.10132.

[10] Dweib MA, Ó Brádaigh CM. Compression molding of glass reinforced thermoplastics: modeling and experiments. Polym Compos 2000;21:832–45. http://dx.doi.org/10.1002/pc.10238.

[11] Dumont P, Vassal J-P, Orgéas L, Michaud V, Favier D, Månson J-AE. Processing, characterisation and rheology of transparent concentrated fibre-bundle suspensions. Rheol Acta 2007;46:639–51. http://dx.doi.org/10.1007/s00397-006-0153-8.

[12] Ericksen JL. Transversely isotropic fluids. Kolloid-Zeitschrift 1960;173:117–22. http://dx.doi.org/10.1007/BF01502416.

[13] Dinh SM, Armstrong RC. A rheological equation of state for semiconcentrated fiber suspensions. J Rheol 1984;28:207–27. http://dx.doi.org/10.1122/1.549748.

[14] Tucker CL. Flow regimes for fiber suspensions in narrow gaps. J Non-Newton Fluid Mech 1991;39:239–68. http://dx.doi.org/10.1016/0377-0257(91)80017-E.

[15] Sommer DE, Favaloro AJ, Pipes RB. Coupling anisotropic viscosity and fiber orientation in applications to squeeze flow. J Rheol 2018;62:669–79. http://dx.doi.org/10.1122/1.5013098.

[16] Görthofer J, Meyer N, Pallicity TD, Schöttl L, Trauth A, Schemmann M, Hohberg M, Pinter P, Elsner P, Henning F, Hrymak AN, Seelig T, Weidenmann K, Kärger L, Böhlke T. Virtual process chain of sheet molding compound: development, validation and perspectives. Compos B 2019;169:133–47. http://dx.doi.org/10.1016/j.compositesb.2019.04.001.
[17] Favaloro AJ, Sommer DE, Denos BR, Pipes RB. Simulation of prepreg platelet compression molding: method and orientation validation. J Rheol 2018;62:1443–55. http://dx.doi.org/10.1122/1.5044533.
[18] Wittemann F, Maertens R, Kärger L, Henning F. Injection molding simulation of short fiber reinforced thermosets with anisotropic and non-Newtonian flow behavior. Compos A 2019;124:105476. http://dx.doi.org/10.1016/j.compositesa.2019.105476.
[19] Schreyer L, Scheuring BM, Christ N, Blarr J, Krauß C, Liebig WV, Weidenmann KA, Böhlke T, Hrymak A, Kärger L. Continuous simulation of a continuous-discontinuous fiber reinforced thermoplastic (CoDiCoFRTP) compression molding process. In: Proceedings of the 2023 international conference on composite materials. Belfast, Northern Ireland; 2024, http://dx.doi.org/10.5445/IR/1000163456.
[20] Song Y, Gandhi U, Pérez C, Osswald T, Vallury S, Yang A. Method to account for the fiber orientation of the initial charge on the fiber orientation of finished part in compression molding simulation. Compos A 2017;100:244–54. http://dx.doi.org/10.1016/j.compositesa.2017.05.021.
[21] Song Y, Gandhi U, Sekito T, Vaidya UK, Vallury S, Yang A, Osswald T. CAE method for compression molding of carbon fiber-reinforced thermoplastic composite using bulk materials. Compos A 2018;114:388–97. http://dx.doi.org/10.1016/j.compositesa.2018.09.002.
[22] Balaji Thattaiparthasarathy K, Pillay S, Ning H, Vaidya UK. Process simulation, design and manufacturing of a long fiber thermoplastic composite for mass transit application. Compos A 2008;39:1512–21. http://dx.doi.org/10.1016/j.compositesa.2008.05.017.
[23] Schreyer L, Blarr J, Höger K, Meyer N, Kärger L. Generation of initial fiber orientation states for long fiber reinforced thermoplastic compression molding simulation. In: Composites meet sustainability : proceedings of the 20th European conference on composite materials. ECCM20, Lausanne, Switzerland; 2022, p. 687–74.
[24] Perez C, Osswald TA, Goris S. Study on the fiber properties of a LFT strand. In: Society of plastics engineers - 13th annual automotive composites conference and exhibition. ACCE 2013, vol. 2, 2013, p. 1115–26.
[25] Song Y, Gandhi U, Sekito T, Vaidya U, Hsu J, Yang A, Osswald T. A novel CAE method for compression molding simulation of carbon fiber-reinforced thermoplastic composite sheet materials. J Compos Sci 2018;2:33. http://dx.doi.org/10.3390/jcs2020033.
[26] Radtke A. Steifigkeitsberechnung von diskontinuierlich faserverstärkten Thermoplasten auf der Basis von Faserorientierungs- und Faserlängenverteilungen [Ph.D. thesis], Stuttgart, Germany: University of Stuttgart; 2009, http://dx.doi.org/10.18419/opus-1788.
[27] Schelleis C, Scheuring BM, Schreyer L, Liebig WV, Hrymak A, Kärger L, Weidenmann KA, Henning F. Process-induced skewness of flow fronts and fiber orientations in LFT-D compression molding considering processing, characterization, and simulation. J Thermoplast Compos Mater 2025;38:2922–44. http://dx.doi.org/10.1177/08927057251344252.
[28] Garesci F, Fliegener S. Young's modulus prediction of long fiber reinforced thermoplastics. Compos Sci Technol 2013;85:142–7. http://dx.doi.org/10.1016/j.compscitech.2013.06.009.
[29] Blarr J. Development of computational, image processing and deep learning methods for the microstructure characterization of carbon fiber reinforced polyamide 6 based on CT images [Ph.D. thesis], Karlsruhe, Germany: Karlsruhe Institute of Technology (KIT); 2024, http://dx.doi.org/10.5445/IR/1000175782.
[30] Scheuring BM. Effect of hybridization in CoDico-FRTPs: Orientation-dependent characterization and analytical modeling in various climatic conditions [Ph.D. thesis], Karlsruhe, Germany: Karlsruhe Institute of Technology (KIT); 2024, http://dx.doi.org/10.5445/IR/1000177112.
[31] Schelleis C, Meckes L, Henning F. Process influences on plastificate and fiber microstructure formation: an LFT-D compression molding parameter study. Solid State Phenom 2026;387:9–19. http://dx.doi.org/10.4028/p-ZoJg4h.
[32] Kanatani K-I. Distribution of directional data and fabric tensors. Internat J Engrg Sci 1984;22:149–64. http://dx.doi.org/10.1016/0020-7225(84)90090-9.
[33] Advani SG, Tucker CL. The use of tensors to describe and predict fiber orientation in short fiber composites. J Rheol 1987;31:751–84. http://dx.doi.org/10.1122/1.549945.
[34] Schultz T, Kindlmann GL. Superquadric glyphs for symmetric second-order tensors. IEEE Trans Vis Comput Graphics 2010;16:1595–604. http://dx.doi.org/10.1109/TVCG.2010.199.
[35] Kass M, Witkin A, Terzopoulos D. Snakes: Active contour models. Int J Comput Vis 1988;1:321–31. http://dx.doi.org/10.1007/BF00133570.
[36] Benson DJ. Computational methods in Lagrangian and Eulerian hydrocodes. Comput Methods Appl Mech Engrg 1992;99:235–394. http://dx.doi.org/10.1016/0045-7825(92)90042-I.
[37] Benson DJ, Okazawa S. Contact in a multi-material Eulerian finite element formulation. Comput Methods Appl Mech Engrg 2004;193:4277–98. http://dx.doi.org/10.1016/j.cma.2003.12.061.
[38] Favaloro AJ, Tseng HC, Pipes RB. A new anisotropic viscous constitutive model for composites molding simulation. Compos A 2018;115:112–22. http://dx.doi.org/10.1016/j.compositesa.2018.09.022.
[39] Meyer N, Ilinzeer S, Hrymak AN, Henning F, Kärger L. Non-isothermal direct bundle simulation of SMC compression molding with a non-Newtonian compressible matrix. J Non-Newton Fluid Mech 2022;310:104940. http://dx.doi.org/10.1016/j.jnnfm.2022.104940.
[40] Mori T, Tanaka K. Average stress in matrix and average elastic energy of materials with misfitting inclusions. Acta Metall 1973;21:571–4. http://dx.doi.org/10.1016/0001-6160(73)90064-3.
[41] Favaloro AJ. The rotation of rigid spheroids in a viscous fluid under mean-field effects. J Non-Newton Fluid Mech 2020;282:104324. http://dx.doi.org/10.1016/j.jnnfm.2020.104324.
[42] Karl T, Böhlke T. Generalized micromechanical formulation of fiber orientation tensor evolution equations. Int J Mech Sci 2024;263:108771. http://dx.doi.org/10.1016/j.ijmecsci.2023.108771.
[43] Folgar F, Tucker CL. Orientation behavior of fibers in concentrated suspensions. J Reinf Plast Compos 1984;3:98–119. http://dx.doi.org/10.1177/073168448400300201.
[44] Jeffery GB. The motion of ellipsoidal particles immersed in a viscous fluid. Proc R Soc Lond Ser A 1922;102:161–79. http://dx.doi.org/10.1098/rspa.1922.0078.
[45] Chung DH, Kwon TH. Invariant-based optimal fitting closure approximation for the numerical prediction of flow-induced fiber orientation. J Rheol 2002;46:169–94. http://dx.doi.org/10.1122/1.1423312.
[46] Meyer N, Schöttl L, Bretz L, Hrymak A, Kärger L. Direct bundle simulation approach for the compression molding process of sheet molding compound. Compos A 2020;132:105809. http://dx.doi.org/10.1016/j.compositesa.2020.105809.
[47] Krauß C, Kärger L. Tensor interpolation in virtual manufacturing chains for fiber reinforced composites. Int J Mech Sci 2022;226:107378. http://dx.doi.org/10.1016/j.ijmecsci.2022.107378.
[48] Shepard D. A two-dimensional interpolation function for irregularly-spaced data. Proceedings of the 23rd ACM national conference. New York City, NY, USA: ACM Press; 1968, p. 517–24. http://dx.doi.org/10.1145/800186.810616.
[49] Favaloro AJ, Sommer DE. On the use of orientation tensors to represent prepreg platelet orientation state and variability. J Rheol 2020;64:517–27. http://dx.doi.org/10.1122/1.5135010.
[50] Dörr D, Singh-Heer N, Gergely RCR, Schreyer L, Henning F, Straatman AG, Hrymak A. Rheological characterization and macroscopic modeling and simulation of the molding process of a PA6 glass mat thermoplastic (GMT). Compos A 2024;176:107780. http://dx.doi.org/10.1016/j.compositesa.2023.107780.
[51] Kapshammer A, Huemer-Kals S, Zulueta K, Fischer P, Major Z. An advanced compression molding simulation and validation of a thick-walled carbon fiber sheet molding compound brake caliper. J Manuf Mater Process 2025;9:137. http://dx.doi.org/10.3390/jmmp9040137.
[52] Schreyer L, Krauß C, Wittemann F, Kärger L. Evaluation of the informed isotropic (IISO) viscosity model for compression molding of discontinuous fiber reinforced polymers. Compos A 2026;203:109552. http://dx.doi.org/10.1016/j.compositesa.2025.109552.